MNRAS 000, 1–14 (2017) Preprint 29 August 2018 Compiled using MNRAS LATEX style file v3.0

XMM-*Newton* and *NuSTAR* joint observations of Mrk 915: a deep look into the X-ray properties⋆

L. Ballo,[1,2]† P. Severgnini,[1] R. Della Ceca,[1] V. Braito,[3,4] S. Campana,[3] A. Moretti,[1] C. Vignali,[5,6] A. Zaino[1,5]

[1]*Osservatorio Astronomico di Brera (INAF), via Brera 28, I-20121, Milano (Italy)*
[2]*XMM-*Newton *Science Operations Centre, ESAC/ESA, PO Box 78, E-28692 Villanueva de la Cañada, Madrid (Spain)*
[3]*Osservatorio Astronomico di Brera (INAF), via E. Bianchi 46, I-23807 Merate, LC (Italy)*
[4]*Department of Physics, University of Maryland, Baltimore County, Baltimore, MD 21250 (USA)*
[5]*Dipartimento di Fisica e Astronomia, Università degli Studi di Bologna, Via Gobetti 93/2, I-40129, Bologna (Italy)*
[6]*Osservatorio Astronomico di Bologna (INAF), Via Gobetti 93/3, I-40129, Bologna (Italy)*

Accepted 2017 May 31. Received 2017 May 31; in original form 2017 February 01

ABSTRACT

We report on the X-ray monitoring programme (covering slightly more than 11 days) carried out jointly by XMM-*Newton* and *NuSTAR* on the intermediate Seyfert galaxy Mrk 915. The light curves extracted in different energy ranges show a variation in intensity but not a significant change in spectral shape. The X-ray spectra reveal the presence of a two-phase warm absorber: a fully covering mildly ionized structure [$\log\xi/(\mathrm{ergs\ cm\ s^{-1}}) \sim 2.3$, $N_{\rm H} \sim 1.3\times10^{21}\,\mathrm{cm^{-2}}$] and a partial covering (~ 90 per cent) lower ionized one [$\log\xi/(\mathrm{ergs\ cm\ s^{-1}}) \sim 0.6$, $N_{\rm H} \sim 2\times10^{22}\,\mathrm{cm^{-2}}$]. A reflection component from distant matter is also present. Finally, a high-column density ($N_{\rm H} \sim 1.5\times10^{23}\,\mathrm{cm^{-2}}$) distribution of neutral matter covering a small fraction of the central region is observed, almost constant, in all observations. Main driver of the variations observed between the datasets is a decrease in the intrinsic emission by a factor of ~ 1.5. Slight variations in the partial covering ionized absorber are detected, while the data are consistent with no variation of the total covering absorber. The most likely interpretation of the present data locates this complex absorber closer to the central source than the narrow line region, possibly in the broad line region, in the innermost part of the torus, or in between. The neutral obscurer may either be part of this same stratified structure or associated with the walls of the torus, grazed (and partially intercepting) the line of sight.

Key words: galaxies: active – X-rays: individual: Mrk 915

1 INTRODUCTION

In the unification paradigm of active galactic nuclei (AGN) by Antonucci (1993), types 1 and 2 AGN classification is a consequence of the inclination angle, more specifically whether the outer molecular torus, supposed to obscure the accretion disk and the broad line region (BLR), intercepts the line of sight. This "static" view, in which the torus is made of a smooth dusty distribution, has been questioned in recent years by several studies (e.g., Elitzur & Shlosman 2006; Nenkova et al. 2008; Hönig & Kishimoto 2010; Merloni et al. 2014). The emerging picture, due to the increasing amount of observations at different wavelengths, requires a more complex structure, maybe clumpy, with multiple absorbers present around the central source at different physical scales (Bianchi et al. 2012; Netzer 2015, and references therein).

Focusing on the X-ray domain, measurements of absorption variability are commonly detected in nearby obscured AGN. These observations imply that the circumnuclear X-ray absorber (or, at least, part of it) must be clumpy, and located at sub-parsec distances from the central source (see e.g., Bianchi et al. 2012), requiring the presence of absorbing gas inside the dust sublimation radius. For NGC 1365, the prototype of AGN showing extreme variations in the X-ray absorbers, the large amount of high-

⋆ Based on observations obtained with the XMM-*Newton* and the *NuSTAR* satellites.
† E-mail: lucia.ballo@gmail.com

quality data from short-timescales monitoring and long observations, allowed to deeply investigate the nature of the absorbing medium. The derived distances and physical parameters, typical of BLR clouds, strongly suggest that the X-ray absorber and the clouds responsible for broad emission lines in the optical/UV are at the same distance from the central black hole (see Risaliti 2016 for a review of the X-ray observations of NGC 1365). Recent observations of NGC 1365 with XMM-*Newton* revealed the presence of a multi-zone warm absorber with different ionization levels (Braito et al. 2014). Indeed, it is nowadays known that the sub-pc/pc scale region of AGN houses also "warm" (i.e., partially photoionized, $T \sim 10^4 - 10^6$ K) gas that absorbs the nuclear emission in the X-ray band. Warm absorbers, observed in at least 50% of the unobscured AGN and quasars, are often found to be complex and multiphase (e.g., Crenshaw et al. 2003; Piconcelli et al. 2004; Porquet et al. 2004; Blustin et al. 2005; McKernan et al. 2007; see Costantini 2010 for a recent review). Outflowing with velocities $\lesssim$ 3000 km/s, these systems possibly originate in a thermally driven wind arising from the inner walls of the molecular torus (Blustin et al. 2005), or represent a later stage of an accretion-disk driven wind (Proga & Kallman 2004). The differently ionized layers of warm absorbers could be part of a single large-scale stratified outflow (Tombesi et al. 2013).

The emerging scenario therefore requires dust-free and dusty clumps that coexist in one physical region that contains the BLR, closer in, and the torus, further away from the central black hole (a recent review can be found in Netzer 2015). Warm gas, possibly outflowing, can contribute to the intercloud BLR medium that provide the pressure confinement for the cold BLR clouds (e.g., Miniutti et al. 2014). In order to investigate the interconnection between these different structures, a powerful tool is to perform X-ray monitoring of AGN observed at intermediate angles, where we expect that the line of sight grazes the torus.

Mrk 915 is a nearby galaxy (z = 0.024) optically classified as Seyfert 1.5 - Seyfert 1.9, depending on the intensity/presence of the broad components of the Hα and Hβ observed at different epochs in the optical spectra (Goodrich 1995; Bennert et al. 2006; Trippe et al. 2010). As summarized in Severgnini et al. (2015), this spectral variability could be due to a change in the reddening level, to a change in the nuclear photoionizing continuum, or to a combination of both. Independently of the origin of this spectral variability, at least part of the optical absorption affecting the central regions originates outside the obscuring torus, and it is most likely associated with the dust lanes seen crossing the central source (Malkan et al. 1998; Muñoz Marín et al. 2007). The stellar disc inclination derived by near-ultraviolet imaging (35° – 57°; Muñoz Marín et al. 2007) implies that in Mrk 915 our line of sight is only partially blocked by the torus, assumed here to be coplanar with the galaxy plane, and with an half-opening angle of $\sim$ 60°. Moreover, in Mrk 915 the torus is likely to have a clumpy structure, as suggested by observations with the Infrared Spectrograph (IRS) on board the *Spitzer* Space Telescope (Mendoza-Castrejón et al. 2015).

In the X-ray, archival *Swift* X-ray Telescope (XRT; Burrows et al. 2005) data strongly suggested the presence of a variable X-ray obscuring medium (Ballo et al. 2014). A daily XRT monitoring programme spanning $\sim$ 3 weeks, presented in Severgnini et al. (2015), allowed us to confirm this hypothesis. We detected a significant count rate variation on a time-scale of a few days, due to a change by a factor $\sim$ 1.5 in the intrinsic nuclear power coupled with a change in the ionization state and/or in the covering factor of a partial covering ionized absorber. The analysis of a $\sim$ 35 ksec *Suzaku* observation of Mrk 915 supports the presence of ionized obscuration (Kawamuro et al. 2016).

In this paper, we present the results from a simultaneous *NuSTAR* and XMM-*Newton* monitoring campaign (covering the 0.3 – 70 keV energy band) performed in 2014 December. The paper is organized as follows. In Section 2 we discuss the X-ray observations and data reduction, while a first comparison between the datasets is presented in Section 3. The X-ray spectral analysis is described in Section 4, with Sections 4.1 and 4.2 devoted to the high energy resolution data and the broadband spectra, respectively. In Section 5 we discuss our results, comparing them with the previous X-ray results, and finally in Section 6 we summarize our work. Throughout the paper we assume a flat ΛCDM cosmology with $H_0 = 71$ km s^{-1} Mpc^{-1}, $\Omega_\Lambda = 0.7$ and $\Omega_M = 0.3$.

2 OBSERVATION AND DATA REDUCTION

2.1 XMM-*Newton*

We observed Mrk 915 with XMM-*Newton* in 2014 December in three pointings (hereafter, OBS 1, OBS 2, and OBS 3; see Table 1), separated from each other by about 5 days, for a total of about 230 ksec (Obs. ID 0744490401, 0744490501 and 0744490601).

The observations were performed with the European Photon Imaging Camera (EPIC), the Optical Monitor (OM) and the Reflection Grating Spectrometer (RGS). In this paper, we concentrate on the data in the X-ray band (EPIC and RGS spectra). The three EPIC cameras (pn, MOS1, and MOS2; Strüder et al. 2001; Turner et al. 2001) were operating in large window mode, with the thin filter applied.

The XMM-*Newton* data have been processed and cleaned using the Science Analysis Software (SAS version 14.0) with the most recent calibrations; the tasks EPPROC and EMPROC were run to produce calibrated and concatenated event lists for the EPIC cameras. EPIC event files have been filtered for high-background time intervals, following the standard method consisting in rejecting time periods of high count rate at energies > 10 keV. A strong flare of $\sim$ 21 ksec is observed during OBS 1, starting at $\sim$ 38 ksec after the beginning of the observation.

Events corresponding to patterns 0 – 12 (MOS1&2) and 0 – 4 (pn) have been used. From the observed count rate, we can exclude event pileup in the EPIC data (see Table 1). The spectral response matrices at the source position were generated using the SAS tasks ARFGEN and RMFGEN and the latest calibration files.

The EPIC source counts were extracted from a circular region of radius 30″ (corresponding to an encircled energy fraction of $\sim$ 90 per cent); background counts were extracted from two source-free circular regions in the same chip of 30″ radius each. Spectra were re-binned with the task SPECGROUP, to not over-sample the instrument energy resolution

Table 1. XMM-*Newton* and *NuSTAR* observation log for Mrk 915.

Obs.	Satellite	Obs. ID	Start	Stop	Detector	Net count rate[a] [counts s^{-1}]	Net exp. time[b] [ks]
	NuSTAR	60002060002	2014-12-02 13:56:07	2014-12-03 18:46:07	FPMA	0.216 ± 0.002	53.0
					FPMB	0.213 ± 0.002	52.9
	XMM-*Newton*	0744490401	2014-12-02 13:54:36	2014-12-04 02:29:18	pn	1.183 ± 0.004	88.9
OBS 1			2014-12-02 14:09:24	2014-12-04 01:48:22	MOS1	0.400 ± 0.002	100.2
			2014-12-02 13:26:16	2014-12-04 02:33:29	MOS2	0.398 ± 0.002	102.0
			2014-12-02 13:25:38	2014-12-03 22:03:56	RGS1-S[c]	0.0121 ± 0.0006	87.5
			2014-12-03 22:31:52	2014-12-04 02:37:33	RGS1-U[c]	0.008 ± 0.002	12.3
			2014-12-02 13:25:46	2014-12-04 02:37:36	RGS2	0.0134 ± 0.0005	101.1
	NuSTAR	60002060004	2014-12-07 06:51:07	2014-12-08 12:46:07	FPMA	0.149 ± 0.002	54.3
					FPMB	0.145 ± 0.002	54.1
	XMM-*Newton*	0744490501	2014-12-07 08:32:29	2014-12-08 02:52:10	pn	0.807 ± 0.004	41.4
OBS 2			2014-12-07 08:13:41	2014-12-08 02:56:17	MOS1	0.269 ± 0.002	51.1
			2014-12-07 08:04:10	2014-12-08 02:56:22	MOS2	0.276 ± 0.002	49.2
			2014-12-07 08:03:31	2014-12-08 03:00:28	RGS1	0.0084 ± 0.0008	49.7
			2014-12-07 08:03:39	2014-12-08 03:00:22	RGS2	0.0090 ± 0.0007	49.7
	NuSTAR	60002060006	2014-12-12 12:41:07	2014-12-13 17:01:07	FPMA	0.118 ± 0.002	50.7
					FPMB	0.106 ± 0.002	50.6
	XMM-*Newton*	0744490601	2014-12-12 13:12:30	2014-12-13 04:17:13	pn	0.718 ± 0.006	22.6
OBS 3			2014-12-12 12:43:41	2014-12-13 04:21:19	MOS1	0.240 ± 0.003	31.9
			2014-12-12 12:44:12	2014-12-13 04:21:24	MOS2	0.243 ± 0.003	32.8
			2014-12-12 12:43:32	2014-12-13 04:25:25	RGS1	0.007 ± 0.001	27.8
			2014-12-12 12:43:40	2014-12-13 04:25:26	RGS2	0.008 ± 0.001	27.6

NOTE: [a] Net source count rate after screening and background subtraction, as observed in the 0.3 – 10 keV (pn, MOS1 and MOS2), 0.5 – 2 keV (RGS1 and RGS2), and 4 – 70 keV (FPMA and FPMB) energy ranges. [b] Net exposure time, after screening was applied on the data. [c] S=scheduled; U=unscheduled.

by more than a factor of three, and to have at least 50 counts in each energy bin. This allows the application of χ^2 statistics.

The RGS (den Herder et al. 2001) data have been reduced using the standard SAS task RGSPROC, and the most recent calibration files; details on net exposure times and total counts are reported in Table 1. After filtering out the high-background time intervals, for each observation we combined the RGS1 and RGS2 spectra (found to be in good agreement, typically to within the 3% level) using the SAS task RGSCOMBINE; the spectra were binned at $\Delta\lambda = 0.1$ Å (slightly undersampling the FWHM spectral resolution).

2.2 *NuSTAR*

NuSTAR (Harrison et al. 2013) observed Mrk 915 simultaneously with XMM-*Newton* with its two co-aligned telescopes with corresponding Focal Plane Modules A (FPMA) and B (FPMB) for a total of about 310 ksec of elapsed time. The level 1 data products were processed with the *NuSTAR* Data Analysis Software (NuSTARDAS) package (ver. 1.4.1). Event files (level 2 data products) were produced, calibrated, and cleaned using standard filtering criteria with the NUPIPELINE task and the latest calibration files available in the NuSTAR calibration database (CALDB). The FPMA and FPMB source counts were extracted from a circular region of radius 60″; this aperture approximates the ≈ 90% encircled-energy fraction contour of the point-spread function. Background counts were extracted from two source-free circular regions of 60″ radius each. *NuSTAR* detects the source above 30 keV with a signal-to-noise ratio of ∼ 13, ∼ 9 and ∼ 7 in OBS 1, OBS 2, and OBS 3, respectively. Spectra were binned in order to have at least 50 counts in each energy bin. Exposure times and total count rates for each spectrum are reported in Table 1.

3 X-RAY VARIABILITY: A FIRST COMPARISON BETWEEN THE DATASETS

We tested time-variability within the XMM-*Newton* and *NuSTAR* observations, generating source light curves in several energy intervals with a binning time of 1000 s (EPIC cameras) and 500 s (FPMs). Fig. 1 (upper panels) shows the X-ray count rate light curves obtained with the EPIC-pn and FPMA in the 0.3 – 1 keV, 1 – 2 keV, 0.3 – 3 keV, 3 – 10 keV and 10 – 70 keV energy ranges. In the lower panels, we present the hardness ratios (HRs) defined as HR=[RATE(H)-RATE(S)]/[RATE(H)+RATE(S)], where RATE(H) and RATE(S) are the count rates observed in the hard and soft bands, respectively. Similar results are obtained if we consider the *NuSTAR* camera FPMB instead of FPMA, and/or the EPIC-MOS data instead of the EPIC-pn. Variations at > 99.9 per cent confidence level (χ^2 test) are observed during OBS 1 and OBS 2 in the XMM-*Newton* data in all intervals above ∼ 1 keV; variations observed during OBS 3 are significant at less than 99.9 per cent confidence level. The *NuSTAR* data do not show statistically

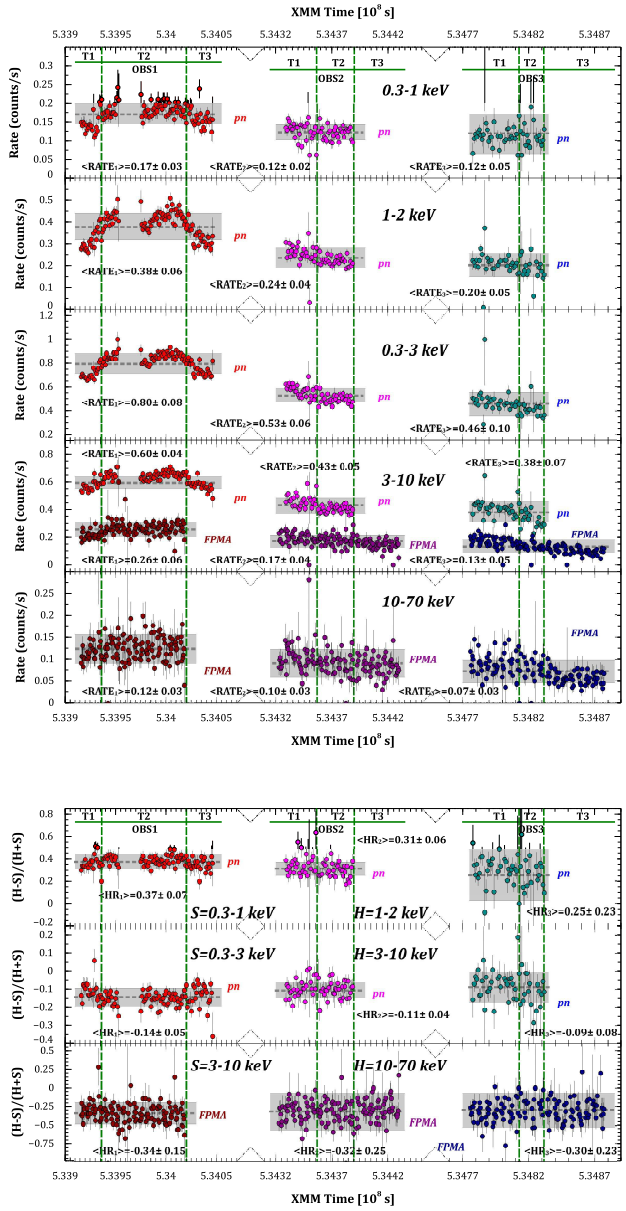

Figure 1. Background-subtracted light curves of Mrk 915 from the XMM-*Newton* pn and the *NuSTAR* FPMA observations (labeled as "OBS 1", "OBS 2" and "OBS 3"; green horizontal lines). Similar results are obtained if we consider the *NuSTAR* camera FPMB instead of FPMA, and/or the EPIC-MOS data instead of the EPIC-pn. For each dataset, we report the mean rate (grey horizontal dashed line) and the standard deviation (shaded area) for the whole observation. The vertical green dashed lines mark the intervals (T1, T2 and T3) in which each observation has been divided (see Sect. 3 and Sect. 4). *Up:* Count rates. From top to bottom: 0.3 – 1 keV, 1 – 2 keV and 0.3 – 3 keV (pn only); 3 – 10 keV (both cameras); 10 – 70 keV (FPMA only). *Down:* Hardness ratios HR=[RATE(H)-RATE(S)]/[RATE(H)+RATE(S)]. Upper panel: H = 1 – 2 keV and S = 0.3 – 1 keV (pn only); middel panel: H = 3 – 10 keV and S = 0.3 – 3 keV (pn only); lower panel: H = 10 – 70 keV and S = 3 – 10 keV (FPMA only).

significant variations, except for observations taken during the OBS 3 period.

In the following analysis, each observation has been divided in three time intervals (labeled as T1, T2 and T3 in Fig. 1), as detailed below. OBS 1 shows the most complex pattern, with a ∼ 35 per cent [∼ 25 per cent] rise in flux observed by XMM-*Newton* between 0.3 and 10 keV [by *NuSTAR* between 3 and 70 keV] during the first ∼ 25 ksec (time interval marked as OBS 1-T1 in Fig. 1). Low-level variations (less than 10 per cent) are observed at time from ∼ 25 to ∼ 70 ksec (OBS 1-T2 interval) both by XMM-*Newton* and *NuSTAR*. After that, the flux lowers until the end of the XMM-*Newton* observation (OBS 1-T3 interval), recovering the initial intensity.

Both OBS 2 and OBS 3 are characterized by a smooth decline over the whole observation, with a ∼ 21 per cent and ∼ 28 per cent drop in the XMM-*Newton* flux, respectively. In these two observations, the separation between T1 and T2 was selected according to a straight line fitted to the count rate observed by XMM-*Newton* in the 0.3 – 10 keV energy range being higher or lower than the mean count rate. The dividing time between T2 and T3 corresponds to the end of the XMM-*Newton* observation (see Fig. 1). *NuSTAR*, observing for longer time intervals, shows a decreasing of ∼ 37 per cent and ∼ 41 per cent in the flux.

However, as shown in the lower panels of Fig. 1, the HR light curves show a lack of significant spectral variability over each observation in each energy band.

Variations between the three observations are clearly visible in all bands, with a drop of ∼ 30 per cent between the mean count rates observed in OBS 1 and OBS 2. A low-level decrease in the mean count rate is observed comparing OBS 2 and OBS 3, with a change of ∼ 13 per cent [∼ 20 per cent] in XMM-*Newton* [*NuSTAR*]. Again, the mean HRs are consistent within the errors (see Fig. 1).

4 X-RAY SPECTRAL ANALYSIS

In this Section we present the analysis of the X-ray spectra of Mrk 915. We first discuss the high-energy resolution data from the RGS, and then we move to the analysis of the XMM-*Newton*-EPIC+*NuSTAR* spectra. Our study of the light curves suggests that during each observation the source vary mainly in flux, since the HR light curves show a lack of significant spectral variability; therefore, to increase the statistics, in the spectral analysis for each observation we consider the time-averaged data over the whole duration. As for the broad-band spectral analysis only, the results obtained on each observation are then compared with the spectra extracted in the relevant T1, T2 and T3 intervals (see Section 3).

Spectral fits were performed using the X-ray spectral fitting package XSPEC (Arnaud 1996) v12.9.0. All the models discussed in the following assume Galactic absorption with a column density of $N_{\rm H,Gal} = 5.3\times10^{20}$ cm^{-2} (Kalberla et al. 2005). To model both Galactic and intrinsic absorptions we used the (Z)TBABS model in XSPEC, adopting cross-sections and abundances of Wilms et al. (2000).

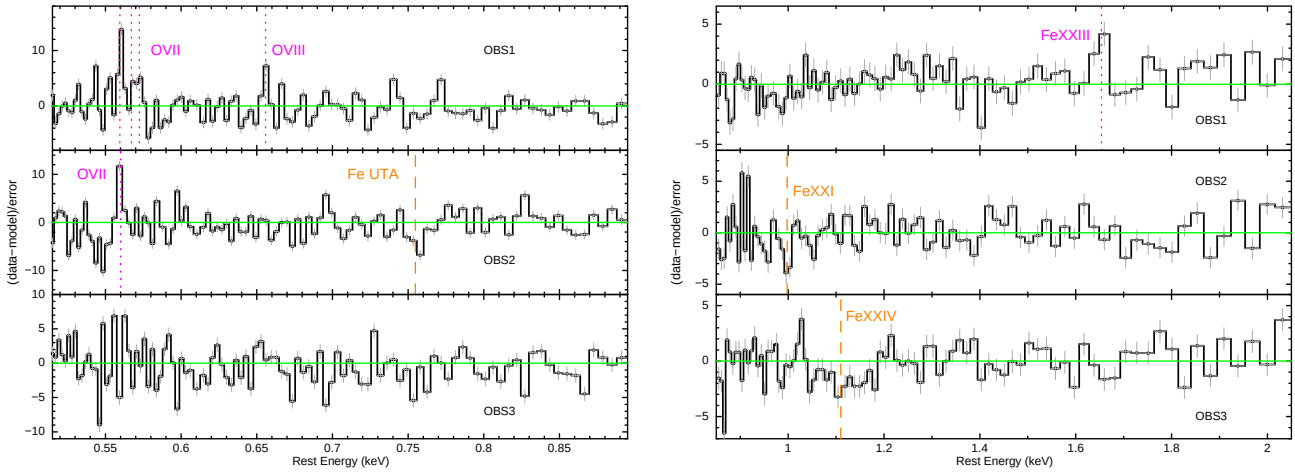

Figure 2. Residuals in the RGS OBS 1 (top), OBS 2 (middle), and OBS 3 (bottom) spectra against the continuum model (from Severgnini et al. 2015, applied to the EPIC+*NuSTAR* data). The data are plotted in the source rest frame, between 0.5 and 0.9 keV (left), and between 0.85 and 2 keV (right). The vertical lines mark the positions of the emission (dotted magenta lines) and absorption (orange dashed lines) features detected during the analysis.

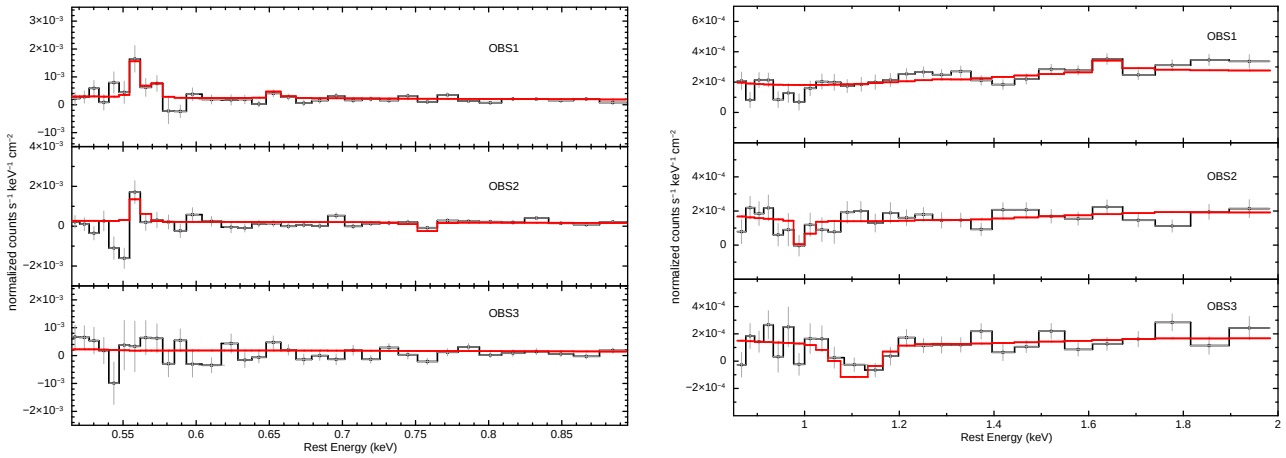

Figure 3. RGS spectra (OBS 1, top; OBS 2, middle; OBS 3, bottom) fitted with the model including an absorbed power law continuum with the detected absorption and emission lines superimposed. The data are plotted in the source rest frame, between 0.5 and 0.9 keV (left), and between 0.85 and 2 keV (right).

4.1 High-resolution RGS data

As a first step, we concentrated on the spectral analysis of the RGS data. The spectra were analyzed over the 0.5 – 2.0 keV energy range, with the *C*-statistic applied (Cash et al. 1979).

The narrow RGS energy range prevents us from performing a detailed spectral fitting of the continuum; an initial guess for its shape was obtained by applying the model describing the *Swift*-XRT data (Severgnini et al. 2015) to the EPIC (0.3 – 10 keV) +*NuSTAR* (4 – 70 keV) data[1]. In Fig. 2 we show the residuals in the RGS data against the resulting continuum. Line-like structures both in emission (at ∼ 0.55 – 0.6 keV and ∼ 1.6 keV) and in absorption (at ∼ 0.75 keV and ∼ 0.9 – 1.2 keV), variable between the observations, are visible.

In order to test the significance of individual features, for each observation we divided the energy ranges on narrow intervals of $\Delta E \sim 0.2 - 0.3$ keV, and subsequently added narrow Gaussian lines to the model; the positions and the normalizations were left free to vary, while the line widths were initially fixed to 2 eV and subsequently (where necessary) were allowed to change. At each step, we also allowed the normalization of the continuum model to vary, while we fixed the parameters of the previously detected lines. The detection of an individual line was considered statistically significant if its addition to the previous model (composed of the absorbed power law with the addition of all the previously detected lines) resulted in an improvement of the fit statistic of $\Delta C > 9.2$ (corresponding to 99% significance level for two parameters of interest), when evaluated in the energy interval considered for the fit. We finally fitted the model composed by the baseline continuum (the partially absorbed power law) plus all the detected absorption and emission lines, over the whole energy range, allowing all the line energies and normalizations to vary, as well as the continuum shape and intensity.

[1] The adopted model is a partially absorbed power law ($N_{\rm H} \sim 2.5 \times 10^{22}$ cm^{-2}, covering factor ∼ 85 per cent).

Table 2 lists the rest-frame energy of the emission (first part) and absorption lines (second part) detected, along with their intensity and the likely identification of the atomic transition (corresponding to the label that identifies each line in Fig. 2). The last three columns list the statistical improvement, the order of inclusion in the model of each line, and the energy interval considered for evaluating the significance of the feature. The final model is shown in Fig. 3.

The observed absorption lines do not show any significant shift in the energy centroid with respect to the known atomic energy. An upper limit on the outflow velocity of $v_{\rm gas} \lesssim 3000\,{\rm km\,s^{-1}}$ can be derived from the 90 per cent errors on the energy centroids. Multiple absorption components may be required in order to model the wide range of ionization states of the gas, covering the Fe Unresolved Transmission Array (UTA) as well as the Fe XXI and higher. An absorption trough likely associated to Fe XVII-XVIII was tentatively detected also in the *Swift*-XRT spectra by Severgnini et al. (2015).

4.2 Broad-band spectral analysis

As anticipated above, in the broad-band spectral analysis we considered the time-averaged data over the whole duration; the results of the analysis are then compared with the spectra extracted in the T1, T2, and T3 intervals, as defined in Sect. 3.

In the broad-band spectral analysis, we kept the FPMA and FPMB spectra separate (following the prescription[2]), while the MOS1 and MOS2 data have been combined together. The MOS, pn, FPMA and FPMB spectra have been fitted simultaneously, keeping the relative normalizations free. The cross-normalization values between EPIC and FPMs were never larger than a few percent, typically of 3 – 5%, as expected (Madsen et al. 2015). We performed the spectral analysis of the EPIC and *NuSTAR* spectra over the energy range from 0.3 keV to 10 keV, and from 4 keV to 70 keV, respectively. Uncertainties are quoted at the 90% confidence level for one parameter of interest ($\Delta\chi^2 = 2.71$).

In Fig. 4 (left panel) we present the OBS 1 (black), OBS 2 (red) and OBS 3 (blue) EPIC-pn and FPMA data, shown as a ratio to a power law ($\Gamma \simeq 1.53$) fitted between 5 keV and 10 keV. The power law normalizations between the observations have been left free to vary. Considering that the MOS and FPMB spectra agree within the errors with the pn and FPMA spectra, respectively, to avoid clutter only data from the last cameras are shown. The model is absorbed by our Galaxy. This plot clearly shows that there is no significant change in the spectral shape between the three observations.

We started the analysis of the broad-band spectra of Mrk 915 with the longest observation of our monitoring, OBS 1. The OBS 2 and OBS 3 datasets were then analysed taking into account the results of the analysis done for the OBS 1 spectra.

The strong decrease in the flux below ~ 5 keV (see Fig. 4, left panel), particularly enhanced between 0.6 and 2 keV, implies the presence of a significant absorption intrinsic to the source. The addition of a neutral absorbing component, both fully or partially covering the nuclear emission, is not able to reproduce the observed spectral shape: in Fig. 4 (right panel) we show the data-to-model ratio obtained by fitting over the whole energy range the OBS 1 data (black symbols) with a power-law component partially covered by a distribution of neutral matter ($\Gamma = 1.61 \pm 0.01$, $N_{\rm H} = (2.5 \pm 0.1) \times 10^{22}\,{\rm cm^{-2}}$, covering factor $CF = 0.90 \pm 0.01$).

By fixing the parameters to the values found for OBS 1, we applied this simple model also to OBS 2 (red symbols in Fig. 4, right panel) and to OBS 3 (blue symbols). The shape of the residuals are similar in all the three observations, confirming that the main driver of the observed variability is a change of the continuum intensity (by a factor of ~ 1.5 – 1.7). Moreover, Fig. 4 clearly highlights that different and/or additional components are required to the fit in order to proper reproduce the global spectral properties of the source during all the monitoring. In particular, a line-like excess around 6.4 keV and a high-energy hump between 10 and 30 keV are visible, suggesting the presence of a reflection component. In the softer part of the spectra (below ~ 3 keV) the presence of different absorption troughs could be indicative that we are intercepting an ionized material along the line of sight, possibly varying during the observations. The presence of ionized materials, previously suggested by the *Swift*-XRT data (Severgnini et al. 2015), is also supported by the RGS results (see Section 4.1).

We first focused on the OBS 1 spectrum at energies > 5 keV. The addition of a Gaussian line to the absorbed power law results in a large improvement in the fit ($\Delta\chi^2$/Δd.o.f. = 262.6/3 between 5 and 10 keV). The profile of the Fe Kα line [$E = 6.42 \pm 0.02$ keV; $\sigma = 86^{+25}_{-24}$ eV; $F = (1.3 \pm 0.2) \times 10^{-5}$ photons cm^{-2} s^{-1}; EW= 125^{+31}_{-25} eV] is marginally resolved. Some residuals at ~ 7.05 keV, the energy where the Fe Kβ line is expected, can be accounted for by adding one more Gaussian line: $E = 7.0 \pm 0.1$ keV; σ tied to the width of the Fe Kα line; EW= 21^{+15}_{-17} eV; flux ~ 14.8 per cent of the Fe Kα (in good agreement with the expectations; Palmeri et al. 2003; Yaqoob et al. 2010), although the improvement in the fit is not statistically significant ($\Delta\chi^2$/Δd.o.f. = 4.5/2 between 5 and 10 keV).

The strength of the Fe Kα line and the possible presence of a Fe Kβ component support the presence of neutral reflection (Reynolds et al. 1994; Matt et al. 1996, 2000). A contribution from a distant reflector was then included in the model by replacing the narrow Gaussian lines with a PEXMON model in XSPEC (Nandra et al. 2007), an additive model self-consistently incorporating the Compton-reflected continuum from a neutral slab combined with emission from Fe Kα, Fe Kβ, Ni Kα and the Fe Kα Compton shoulder. During the fits, we tied the PEXMON photon index and normalization to that of the primary power law, and we fixed the cutoff energy at 100 keV, the abundances of heavy elements at their Solar values, and the inclination angle at 55° (Severgnini et al. 2015, see also Keel 1996; Muñoz Marín et al. 2007). The only free parameter of the PEXMON component was the reflection scaling factor, found to be $\mathcal{R} = 0.62 \pm 0.08$ ($\chi^2_{\rm r} = 1.151$).

There is a small disagreement in photon index ($\Delta\Gamma \sim 0.07$) between the XMM-*Newton* and *NuSTAR* instruments,

[2] http://www.nustar.caltech.edu/page/response_files; see also https://heasarc.gsfc.nasa.gov/docs/nustar/analysis, "*NuSTAR* Analysis Caveats"

Table 2. Combined XMM-*Newton*-RGS1 and RGS2: best-fit absorption and emission lines required.

Emission Lines								
Obs. (1)	Rest E (2)	Intensity (3)	σ (4)	ID (5)	Atomic E (6)	ΔC (7)	Sequence (8)	$\Delta E_{\rm fit}$ (9)
OBS 1	0.560 ± 0.001	$2.95^{+1.71}_{-1.59}$	2^f	O VII Heα (f)	0.561	$18.1^{\dagger}$	I	0.5 – 0.7
	0.568^t	< 1.33	2^f	O VII Heα (i)	0.569			
	0.573^t	< 1.97	2^f	O VII Heα (r)	0.574			
	0.656 ± 0.002	$0.56^{+0.38}_{-0.36}$	2^f	O VIII Lyα	0.653	9.8	II	0.6 – 0.8
	$1.654^{+0.058}_{-0.017}$	$0.64^{+0.51}_{-0.54}$	2^f	Fe XXIII	1.659	9.4	III	1.5 – 1.8
OBS 2	0.560 ± 0.002	$2.85^{+2.04}_{-1.76}$	2^f	O VII Heα	0.561 – 0.574	11.7	I	0.5 – 0.7

Absorption Lines								
Obs. (1)	Rest E (2)	Intensity (3)	σ (4)	ID (5)	Atomic E (6)	ΔC (7)	Sequence (8)	$\Delta E_{\rm fit}$ (9)
OBS 2	$0.755^{+0.007}_{-0.003}$	$-\left(1.14^{+1.64}_{-0.89}\right)$	2^f	Fe UTA	0.729 – 0.775	9.4	III	0.65 – 0.85
	$0.998^{+0.010}_{-0.009}$	$-\left(0.69^{+1.82}_{-0.40}\right)$	< 32	Fe XXI	0.995	9.3‡	II	0.95 – 1.1
OBS 3	$1.110^{+0.026}_{-0.015}$	$-\left(3.06^{+3.86}_{-1.47}\right)$	< 34	Fe XXIV	1.110	11.2‡	I	1 – 1.3

Note: The statistic for the best-fit model [for the model with no lines] is C/d.o.f. = 187.4/174 [C/d.o.f. = 217.2/182], C/d.o.f. = 206.4/173 [C/d.o.f. = 284.1/180] and C/d.o.f. = 192.4/179 [C/d.o.f. = 203.1/181], for OBS 1, OBS 2 and OBS 3, respectively. f = parameter fixed during the fit. t = tied to the energy of the O VII Heα forbidden component ($E_{\rm r} - E_{\rm f} = 0.013$ keV and $E_{\rm i} - E_{\rm f} = 0.008$ keV). † Δd.o.f = 4. ‡ Δd.o.f = 3. Column (1): observation. Column (2): measured line energy in the source rest frame, in units of keV. Column (3): line normalization, in units of 10^{-5} photons cm^{-2} s^{-1}. Column (4): line width, in units of eV. Column (5): possible identification; forbidden, intercombination, and resonance lines denoted by (f), (i), and (r). Column (6): known atomic energy of the most likely identification of the line, in units of keV. Column (7): improvement in C-statistic (considering only the bins in the energy interval of $\Delta E \sim 0.2 - 0.3$ keV around the line centroid quoted in Column 8) upon adding the line (Δd.o.f = 2) with respect to the baseline model with the addition of the lines detected in the previous steps. Column (8): detection sequence. Column (9): Energy range considered for the fit, in units of keV.

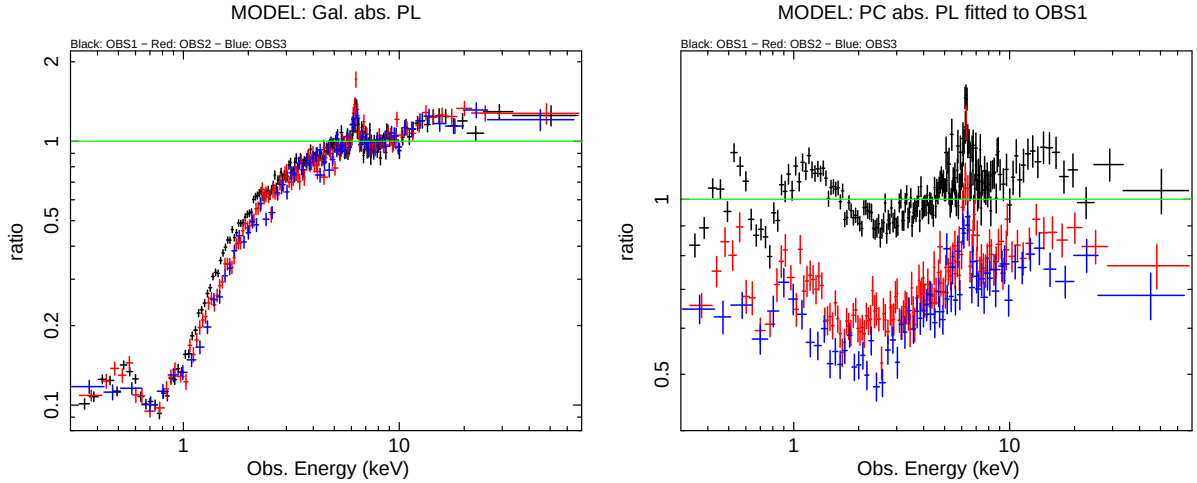

Figure 4. Data-to-model ratio for the XMM-*Newton* pn and *NuSTAR* FPMA spectra: black, OBS 1; red, OBS 2; blue, OBS 3. All data are rebinned for clarity. *Left:* the model is a power law, fitted to the data between 5 and 10 keV ($\Gamma \sim 1.53$), absorbed by our Galaxy. *Right:* a partial covering neutral absorber is added to the model and fitted to the OBS 1 data considering the whole energy range.

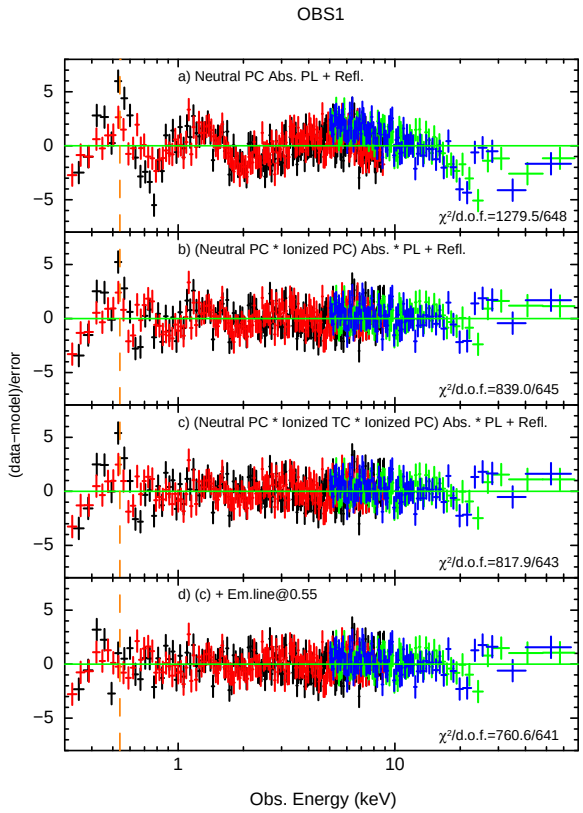

Figure 5. Relevant residuals, plotted in terms of sigmas with error bars of size one, when different models are applied to the XMM-*Newton* (black, pn; red, MOS) and *NuSTAR* (green, FPMA; blue, FPMB) spectra of Mrk 915 as recorded during the OBS 1 observation: from top to bottom, a continuum composed by the intrinsic power law and a reflection component is view through a partially covering neutral absorber (panel a); in panel b) we present the residuals when a partially covering ionized absorber is included, while in panel c) a second ionized layer has been added. Finally, panel d) shows the residuals when the model includes also the soft X-ray emission line; its position is marked in all panels with a vertical orange dashed line. All data are rebinned for clarity.

as previously reported for other simultaneous observations (e.g., Parker et al. 2016; Cappi et al. 2016). In order to take into account the remaining calibration uncertainties, in the following we allowed to vary the photon index between the satellites. Here and below, we report Γ and fluxes obtained for the XMM-*Newton* only.

We then extended the analysis to the whole energy interval covered by the data, where we still have a poor fit below $\sim 3-4$ keV (χ^2/d.o.f. = 1279.5/648; see Fig. 5, panel a). Line-like structures, both in emission and in absorption, typically observed in partially/fully ionized absorber(s) flowing along the light of sight, could explain the observed residuals in the soft energy range. Absorption features at $E \sim 0.8$ keV associated with the presence of warm absorbers have been already detected in the *Swift*-XRT spectra of Mrk 915 (Severgnini et al. 2015). Since the presence of these components is also supported by the RGS data, we added a ionized absorber. To model the absorption in Mrk 915 in a physically consistent way, we used a grid of photoionized absorbers generated with the XSTAR[3] photoionization code (Kallman et al. 2004) assuming turbulence velocity of $\sigma = 100$ km s^{-1}. This latter value is consistent with the narrow, or unresolved, widths of the absorption lines detected in the RGS spectra (see Section 4.1). The adopted XSTAR table assumes a power-law continuum ($\Gamma = 2$) from 0.0136 to 13.6 keV ionizing a constant density shell of gas with standard solar abundances. The free parameters of this component are the absorber column density $N_{\rm H}$ and the ionization parameter[4] $\log\xi/(\mathrm{ergs\ cm\ s^{-1}})$, varying in the ranges $10^{20}-10^{24}$ cm^{-2} and $0-6$, respectively.

The results of the fit with two partially covering absorbers applied are a low-ionization state, $\log\xi/(\mathrm{ergs\ cm\ s^{-1}}) = 0.71 \pm 0.01$, with $N_{\rm H} = (1.97 \pm 0.02) \times 10^{22}$ cm^{-2}, and a covering fraction[5] $\simeq 0.94$; and a higher column density [$N_{\rm H} = (1.583^{+0.120}_{-0.127}) \times 10^{23}$ cm^{-2}] neutral absorber covering 35^{+3}_{-2}% of the central source. The improvement in the fit is significant (χ^2/d.o.f. = 840.0/645); however, residuals below ~ 2 keV are still visible (Fig. 5, panel b). We thus tested the presence of one more layer of matter. This additional absorber, slightly more ionized [$\log\xi/(\mathrm{ergs\ cm\ s^{-1}}) = 2.39^{+0.14}_{-0.09}$] has a lower column density [$N_{\rm H} = (1.9^{+1.1}_{-0.7}) \times 10^{21}$ cm^{-2}], and a covering fraction consistent with the unity; therefore, in the following analysis, we assumed that this absorber fully covers the whole emission. The addition of the second layer improves the fit by $\Delta\chi^2/\Delta$d.o.f. = 21.1/2 (Fig. 5, panel c; see in particular at $E < 2$ keV). We note that the presence of two layers of matter with different ionization states is suggested also by the high energy-resolution RGS data (see Section 4.1). During the fit, both ionized absorbers have been assumed to be steady; allowing their velocities to vary, we found in both cases $v_{\rm out} < 1000$ km/s, with no significant improvement in the fit. Finally, residuals below ~ 1 keV require the addition of an emission line (parametrized with a narrow Gaussian, σ fixed to 5 eV) to be accounted for. The improvement in the fit is significant ($\Delta\chi^2/\Delta$d.o.f. = 57.3/2; see Fig. 5, panel d); the energy is $E = 0.55 \pm 0.01$ keV, with EW= 39^{+14}_{-16} eV and $F = (2.9^{+0.8}_{-0.9}) \times 10^{-3}$ photons cm^{-2} s^{-1}.

In Fig. 6 (upper panel) we have plotted the unfolded best fit to the XMM-*Newton* and *NuSTAR* data obtained with this combination of neutral and ionized absorbers and emission line, with the addition of reflection from distant matter; in the second panel we show the residuals between the data and the best-fitting model. This complex model resulted in a roughly acceptable description of the data (χ^2/d.o.f. = 760.6/641); the best fit parameters are shown in Table 3.

[3] http://heasarc.gsfc.nasa.gov/docs/software/xstar/xstar.html
[4] The ionisation parameter is defined as $\xi = L_{\rm ion}/nR^2$, where n is the hydrogen number density of the gas (in cm^{-3}) and R is the radial distance of the absorbing/emitting material from the central source of X-ray (in cm), while $L_{\rm ion}$ is the ionising luminosity (in ergs s^{-1}) integrated between 1 Ryd and 1000 Ryd (1 Ryd = 13.6 eV).
[5] We define the covering fracion as the complement to one of the ratio between the normalizations of the unabsorbed and absorbed power laws.

Table 3. Analysis of the broad band XMM-*Newton*-EPIC (0.3 – 10 keV) and *NuSTAR* (4 – 70 keV) spectra: result for a partial covering neutral absorber∗{ionized absorber∗[partial covering ionized absorber∗(intrinsic power law)]+reflection from distant matter+narrow line} model.

	Direct and Reflected Continua			Neutral and Ionized Absorbers			Gaussian		
Obs.	Γ	Norm	$\mathcal{R}$	$N_{\rm H}$	$\log\xi$	Cov. fraction	$E_{\rm rf}$	EW	χ^2/d.o.f.
(1)	(2)	(3)	(4)	(5)	(6)	(7)	(8)	(9)	(10)
OBS 1	1.86 ± 0.03	$2.89^{+0.22}_{-0.16}$	0.68 ± 0.08	$14.37^{+2.94}_{-1.51}$	–	$0.33^{+0.02}_{-0.03}$	0.55 ± 0.01	39^{+14}_{-16}	760.6/641
				$0.13^{+0.14}_{-0.08}$	$2.31^{+0.28}_{-0.40}$	1^{f}			
				$1.92^{+0.05}_{-0.03}$	$0.65^{+0.01}_{-0.09}$	0.94 ± 0.01			
OBS 2	$1.82^{+0.03}_{-0.02}$	$1.88^{+0.08}_{-0.03}$	$0.60^{+0.05}_{-0.07}$	$14.37^{+3.20}_{-3.46}$	–	0.33 ± 0.02	0.56 ± 0.01	49^{+36}_{-14}	658.6/553
				$0.03^{+0.10}_{-0.01}$	< 2.34	1^{f}			
				1.67 ± 0.03	$0.43^{+0.02}_{-0.13}$	0.92 ± 0.01			
OBS 3	1.85 ± 0.01	$1.86^{+0.04}_{-0.03}$	$0.54^{+0.13}_{-0.10}$	$15.28^{+4.80}_{-4.38}$	–	$0.31^{+0.03}_{-0.05}$	$0.56^{+0.05}_{-0.09}$	< 40	479.0/463
				< 5.25	< 3.14	1^{f}			
				$2.33^{+0.09}_{-0.06}$	$0.59^{+0.15}_{-0.08}$	0.92 ± 0.01			

Note: Errors are quoted at the 90% confidence level for 1 parameter of interest ($\Delta\chi^2 = 2.71$). f = parameter fixed during the fit. The neutral Compton reflection, described using the pexmon model in xspec include, self-consistently both the continuum and the Fe and Ni emission lines. Column (1): observation. Column (2): intrinsic power law and reflection component photon index. Column (3): intrinsic power-law normalization, in units of 10^{-3} photons keV^{-1} cm^{-2} s^{-1} @1 keV. Column (4): reflection fraction, with respect to the intrinsic continuum observed during OBS 1. Column (5): warm absorber column density, in units of 10^{22} cm^{-2}. Column (6): ionization parameter $\xi = L_{\rm ion}/nR^2$ (in units of ergs cm s^{-1}), where $L_{\rm ion}$ is the ionising luminosity (in units of ergs s^{-1}), n is the hydrogen number density of the gas (part cm^{-3}) of the illuminated slab, and R is the radial distance of the absorbing/emitting material from the central source of X-ray (in cm). Column (7): complement to one of the uncovered-to-covered flux ratio. Column (8): rest-frame energy centroid of the Gaussian emission line (width fixed to 50 eV), in units of keV. Column (9): emission line equivalent width, in units of eV. Column (10): χ^2 and number of degrees of freedom.

Table 4. X-ray fluxes and luminosities.

	Observed Flux			Intrinsic Luminosity			
Obs.	0.3-2 keV	2-10 keV	10-70 keV	0.3-2 keV	2-10 keV	10-70 keV	0.0136-13.6 keV
OBS 1	$0.96^{+0.11}_{-0.06}$	7.66 ± 0.60	$19.85^{+1.86}_{-1.90}$	$10.53^{+0.63}_{-0.74}$	$11.21^{+0.67}_{-0.79}$	$18.53^{+1.11}_{-1.31}$	$36.88^{+2.20}_{-2.60}$
OBS 2	$0.64^{+0.02}_{-0.08}$	$5.49^{+0.23}_{-0.25}$	$13.70^{+0.07}_{-0.08}$	$6.66^{+0.27}_{-0.09}$	$7.68^{+0.31}_{-0.11}$	$11.67^{+0.47}_{-0.16}$	$23.30^{+0.94}_{-0.32}$
OBS 3	0.56 ± 0.02	$5.02^{+0.22}_{-0.17}$	$13.56^{+1.10}_{-0.85}$	$6.64^{+0.14}_{-0.10}$	$7.34^{+0.16}_{-0.11}$	$11.88^{+0.25}_{-0.18}$	$23.21^{+0.49}_{-0.35}$

Note: Errors are quoted at the 90% confidence level for 1 parameter of interest ($\Delta\chi^2 = 2.71$). Luminosity are absorption-corrected, while fluxes are corrected only for the Galactic absorption. Fluxes (in units of 10^{-12} ergs cm^{-2} s^{-1}) and luminosities (in units of 10^{42} ergs s^{-1}) refer to the pn.

4.3 The origin of the X-ray variability: comparison among the different datasets

Having found a physical scenario able to describe the OBS 1 data, we explored the possibility of explaining the variability observed by changing only the best fit parameters (but assuming the same components in the model): therefore, we applied the model described in Sect. 4.2 to the OBS 2 and OBS 3 datasets.

As a first step, we fitted the data twice, by leaving free to vary the intrinsic power-law normalization only or the warm absorbers parameters only, respectively. We found that the observed variations can be attributed mainly to a decreasing of a factor $\sim 1.5 - 1.7$ of the direct continuum, although residuals observed below ~ 2 keV are indicative of some variations occurred in the absorbing medium(s).

This is confirmed also by analysing the OBS 2 and OBS 3 states leaving free to vary all the different components of the model. Note that, to better compare the reflection fractions in the three observations, both OBS 2 and OBS 3 data have been fitted by fixing the normalization of the pexmon model to the value of OBS 1. The best fit value for the parameters are reported in Table 3, while Fig. 7 and Fig. 8 show the unfolded spectra (upper panel) and the residuals (second panel) for OBS 2 (χ^2/d.o.f. = 658.6/553) and OBS 3 (χ^2/d.o.f. = 479.3/463), respectively. Table 4 presents the observed fluxes (corrected for Galactic absorption) and unabsorbed luminosities for the three observations.

As discussed in Sect. 3, small but statistically significant variations are observed in different energy ranges during each observation, although with substantially constant HRs. For each observation, we applied the model discussed so far to the datasets collected in the T1, T2, and T3 intervals, as marked in Fig. 1. By fitting the data jointly, we tried to reproduce the data leaving free to vary between the single intervals the intrinsic power-law normalization only or the absorbers parameters only. We found that a variation in the intrinsic continuum is always required, confirming that also during each observation a change in the continuum intensity of a factor C (with respect to the mean spectrum) ranging from ~ 1.14 to ~ 0.55 is the main driver of the light-curve properties. The relevant residuals are plotted in the last three panels of Fig. 6 (OBS 1), Fig. 7 (OBS 2) and Fig. 8 (OBS 3).

Finally, we tested the EPIC+*NuSTAR* best-fit model with the RGS spectra. The data do not allow us to properly fit such a complex model, therefore we allowed only one absorbing layer to vary at each time, keeping the remaining components fixed to the best fit values re-

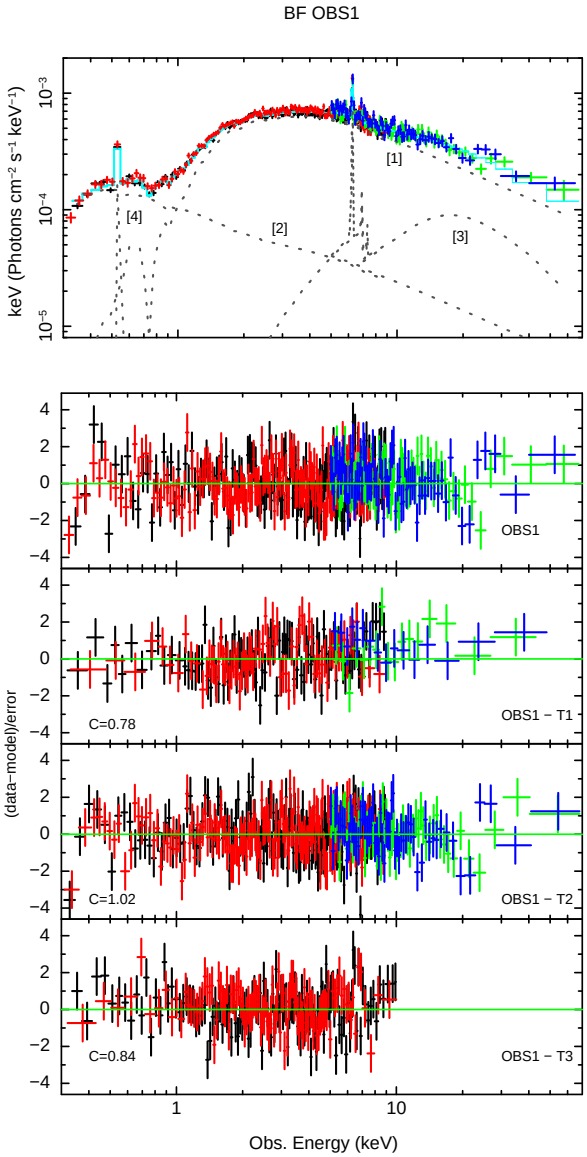

Figure 6. Upper panel: unfolded XMM-*Newton* (black, pn; red, MOS) and *NuSTAR* (green, FPMA; blue, FPMB) spectra of Mrk 915 as recorded during the whole OBS 1 period, with the best-fit model applied (cyan continuous line): intrinsic power law partially covered by a warm absorber ([1] and [2] identify the fraction of continuum covered and uncovered, respectively) seen through a second ionized layer of material, plus reflection from distant material [3] and narrow emission line [4]; the whole emission is absorbed by neutral material partially covering the central region. Lower panels, from top to bottom: relevant residuals, plotted in terms of sigmas with error bars of size one, when the model is applied to the spectra observed during the whole OBS 1 period (same as in Fig. 5, panel d), and to the three time intervals marked in Fig. 1 (as labelled), assuming a change in the intensity of the intrinsic continuum of a factor C (with respect to the mean spectrum).

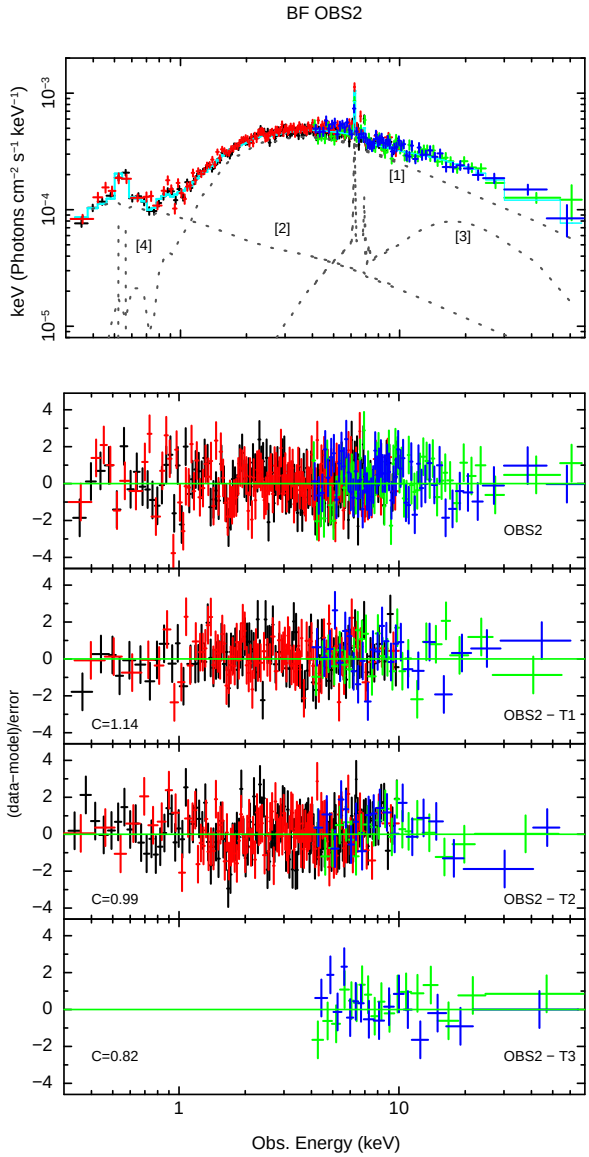

Figure 7. As in Fig. 6, but for the OBS 2 period.

ported in Table 3. We found ionization parameters and column densities broadly consistent with the values previously derived. For the partially-covering absorber we found $\log\xi/(\mathrm{ergs\ cm\ s^{-1}}) = 0.63^{+0.04}_{-0.08}$, $N_{\rm H} = (2.0 \pm 0.1) \times 10^{22}\,\mathrm{cm^{-2}}$; $\log\xi/(\mathrm{ergs\ cm\ s^{-1}}) = 0.6^{+0.1}_{-0.2}$, $N_{\rm H} = (2.1^{+0.4}_{-0.2}) \times 10^{22}\,\mathrm{cm^{-2}}$; $\log\xi/(\mathrm{ergs\ cm\ s^{-1}}) < 0.5$, $N_{\rm H} = (1.5^{+0.6}_{-0.3}) \times 10^{22}\,\mathrm{cm^{-2}}$, for OBS 1, OBS 2 and OBS 3, respectively. While for the total covering absorber we obtained: $\log\xi/(\mathrm{ergs\ cm\ s^{-1}}) < 1.7$, $N_{\rm H} < 5 \times 10^{21}\,\mathrm{cm^{-2}}$; $\log\xi/(\mathrm{ergs\ cm\ s^{-1}}) < 1$, $N_{\rm H} < 3 \times 10^{21}\,\mathrm{cm^{-2}}$; $\log\xi/(\mathrm{ergs\ cm\ s^{-1}}) < 1$, $N_{\rm H} < 4 \times 10^{21}\,\mathrm{cm^{-2}}$, for OBS 1, OBS 2 and OBS 3, respectively.

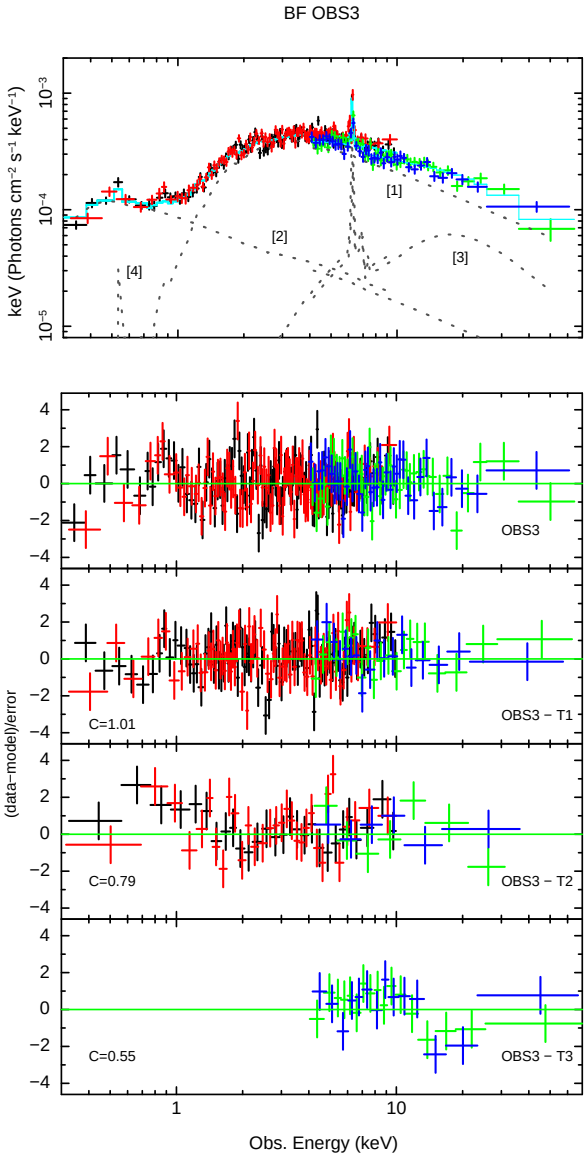

Figure 8. As in Fig. 6, but for the OBS 3 period.

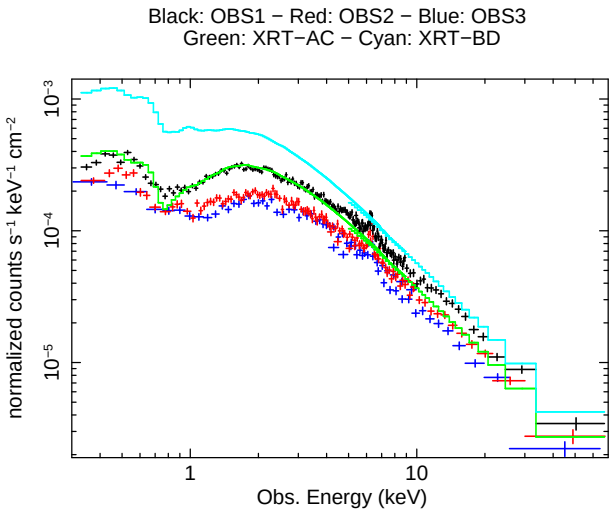

Figure 9. XMM-*Newton* and *NuSTAR* spectra (black, OBS 1; red, OBS 2; blue, OBS 3) compared with the two emission states observed during the *Swift*-XRT monitoring, as analysed in Severgnini et al. (2015, green, low state; cyan, high state).

5 DISCUSSION

We have presented a detailed spectral analysis of the XMM-*Newton* + *NuSTAR* monitoring of Mrk 915, covering slightly more than 11 days.

Several features are clearly evident in the low energy resolution spectra of Mrk 915 (see Fig. 4): a strong absorption between ∼ 0.7 and ∼ 3 keV, a spectral flattening at lower energies, emission-line residuals in the iron band, and a bump at energies higher than ∼ 10 keV. Moreover, variations in intensity in the soft, medium, and hard energy ranges, but not in spectral shape are clearly seen (see Fig. 1). However, the level of variation is much lower than observed in the previous *Swift*-XRT monitoring (Severgnini et al. 2015): in Fig. 9 we compare our new data with the models which provide the best fit to the two states identified in the XRT data. As evident, the new monitoring finds the source at an emission level comparable with the low state observed by XRT, while the high XRT state is never reached.

The analysis of the RGS data provides an hint for the presence of a multi-layer partially ionized absorber, as previously suggested by Severgnini et al. (2015); a few emission lines are also detected. The 0.3 – 70 keV XMM-*Newton*-EPIC and *NuSTAR* spectra have been analyzed in the framework of an "absorption-based" scenario. In our best-fit broad-band model, the primary power-law emission is partially covered (covering fraction ∼ 0.9) by a low ionization ($\xi \sim 3-5$ ergs cm s^{-1}) warm absorber, and totally covered by a mildly-ionized ($\xi \lesssim 200$ ergs cm s^{-1}) absorber. A relatively small fraction (covering factor ∼ 0.3) of the whole emission is absorbed by a rather high ($\sim 1.5\times10^{23}$ cm^{-2}) column density of neutral gas. A narrow Gaussian emission line, consistent with Kα fluorescence from almost neutral iron, accounts for the residuals observed between 6 and 7 keV, while the reflection component expected to be associated to the line can reproduce the spectral curvature observed at high energy. Finally, a narrow emission line is detected at ∼ 0.56 keV; the most likely identification of this feature is the O VII Heα. The presence of this line is supported also by the RGS data.

Given the complexity of the multi-component spectral model used here, we do not expect that the observed spectral variability could be ascribed to a single parameter alone, but rather to several parameters combined. In Fig. 10 we plot the evolution of the spectral fit parameters. Passing from OBS 1 to OBS 2 and OBS 3 observations, the direct continuum decreased significantly, as evident from the top-left panel where we plot the intrinsic 7 – 10 keV flux light curve: the flux in this energy band should have very little, if any, sensitivity to the obscuration. The strength of the reflection component is basically constant: the reflection fraction is consistent between the three periods ($\mathcal{R}_{\rm OBS\,1} = 0.68 \pm 0.08$, $\mathcal{R}_{\rm OBS\,2} = 0.60^{+0.05}_{-0.07}$, and $\mathcal{R}_{\rm OBS\,3} = 0.54^{+0.13}_{-0.10}$, see Table 3), implying that this component does not respond to the variation of the direct emission, in agreement with an origin of the reflection in rather distant matter.

In addition, slight variations in the column density and ionization state of the partially-covering absorber are observed (right column in Fig. 10). As regards the second ionized absorber, instead, the data are consistent with a substantially constant component, although poorly constrained in OBS 2 and OBS 3 (third column in Fig. 10). Finally, as evident in the second column of Fig. 10, the neutral absorber does not change between the observations.

Despite being a clear over-parametrization of the *Swift*-XRT data, the same model can be used to satisfactorily reproduce also the two *Swift*-XRT states. We fixed the components of the model that, from our analysis of the XMM-*Newton*+*NuSTAR* monitoring, are consistent with being constant: the reflection component, the neutral absorber, and the total covering ionized absorber. With these assumptions, the change from the low to the high state can be explained by a concomitant variation in the intrinsic flux of a factor ~ 1.6 and a change of the column density of the partially covering low-ionized absorber ($\Delta N_{\rm H} \sim 5 \times 10^{21}$ cm^{-2}).

In the following we will try to set some plausible constraints on the location R of the two ionized absorbers as a function of the density of the medium n using the relation with the ionization luminosity and the ionization parameter, $\xi = L_{\rm ion}/nR^2$. As for the total covering mildly-ionized absorber we focus on OBS 1, since this is the only observation in which the parameters of this component are well-constrained (see Table 3). We estimated a ionizing luminosity between 13.6 eV and 13.6 keV, $L_{\rm ion,OBS\,1} \sim 3.7 \times 10^{43}$ ergs s^{-1} (see Table 4), thus implying:

$$nR^2 = 2 \times 10^{41}\ {\rm cm}^{-1} \quad (1)$$

As for the partially-covering low-ionized layer, from the best-fit values found for each observation as reported in Table 3, and given the corresponding ionizing luminosities between 13.6 eV and 13.6 keV observed during the monitoring, $L_{\rm ion} \sim (2.3 - 3.7) \times 10^{43}$ ergs s^{-1} (see Table 4), we have:

$$nR^2 = (6 - 9) \times 10^{42}\ {\rm cm}^{-1} \quad (2)$$

By considering typical density values for the BLR ($n_{\rm BLR}$), the torus ($n_{\rm torus}$) and the NLR ($n_{\rm NLR}$), we checked if the values of R derived by equations 1 and 2 are consistent with the expected distances of these regions from the central AGN in Mrk 915. For a typical BLR density $n_{\rm BLR} > 10^8$ cm^{-3} (Osterbrock 1989; Netzer 2013) we obtain $R \lesssim 4 \times 10^{16}$ cm and $R \lesssim 3 \times 10^{17}$ cm for the total and the partial covering absorbers, respectively. These values are consistent with the distance of the BLR as estimated from the optical luminosity ($R_{\rm BLR} \approx 10^{16}$–$10^{17}$ cm; Severgnini et al. 2015). Similarly, by assuming $n_{\rm torus} \sim 10^6$ cm^{-3} (Netzer 2013), the derived distances are $R \sim 4 \times 10^{17}$ cm and $R \sim 3 \times 10^{18}$ cm for the total and the partial covering absorbers, respectively, in good agreement with the inner radius of a torus as derived from observations in the infrared (pc-scale, see e.g. Jaffe et al. 2004, and the discussion in Burtscher et al. 2013). Assuming instead the NLR density quoted by Bennert et al. (2006) for Mrk 915, $n_{\rm NLR} \sim 500$–1000 cm^{-3}, we find $R \sim (1$–$2) \times 10^{19}$ cm and $R \sim (0.8 - 1) \times 10^{20}$ cm (total and partial covering absorbers, respectively). These values are about a factor 800 – 100 lower than the radius of the NLR estimated by the same authors, $R_{\rm NLR} \sim 8 \times 10^{21}$ cm.

These considerations imply that the two ionized absorbers could be part of the BLR or they could be distributed between the BLR and the inner part of the neutral torus, well inside the radius of the NLR.

Similar, but less stringent, results can be obtained under the reasonable assumption of the thickness of each layer $\Delta R \sim N_{\rm H}/n$ lower than R. In this case, we can derive an upper limit to the distance $R < L_{\rm ion}/(N_{\rm H}\xi)$: we found $R < 1.4 \times 10^{20}$ cm and $R < 5.2 \times 10^{20}$ cm for the totally-covering and the partially-covering absorbers, respectively, well within the NLR in Mrk 915. Multi-layer absorbers, possibly stratified, characterized by different ionization states and densities, located at distances ranging from tens to hundreds of parsecs from the central source have been detected in several Seyfert galaxies (see e.g. Ebrero et al. 2010, 2013).

As for the neutral absorber, the high column density, low covering factor and constancy of this component can suggest its association with the circumnuclear torus. In this case, as suggested by Severgnini et al. (2015), our line of sight likely grazes (and partly intercepts) the walls of the torus, providing us a favoured perspective to detect internal multi-zone ionized absorbers.

An alternative possibility is that all the different absorbers, neutral and ionized, here detected are part of the same obscuring medium: it would consist of a mix of gas with different temperature and density, as observed e.g. in NCG 5548 (Kaastra et al. 2014).

Unfortunately, with the present data we are not in the position to discriminate between these different scenarios.

6 CONCLUSIONS

We have performed a broad-band monitoring programme of Mrk 915, observed jointly with the XMM-*Newton* and *NuSTAR* satellites. The programme consists of 3 observations separated from each other by about 5 days. The main results of this work can be summarized as follows.

(i) This monitoring found Mrk 915 in an emission level comparable with the low state observed by *Swift*-XRT (Severgnini et al. 2015), while the high XRT state is never reached. Comparing the X-ray light curves in the soft (0.3 – 1 keV, 1 – 2 keV, and 0.3 – 3 keV), medium (3 – 10 keV) and hard (10 – 70 keV) energy bands, we found variations in intensity, but not in spectral shape. The strongest variation is observed between OBS 1 and OBS 2, when the count rate decreases by a factor of ~ 1.4.

(ii) The high energy resolution data collected by the RGS suggest the presence of a multi-layer partially ionized absorber. A few emission lines are also observed.

(iii) As for the low-resolution spectra, the importance of absorption structures is evident in all datasets. The three states can be well described within an "absorption-based" scenario, fully consistent with the results obtained from the RGS data: an intrinsic power law with photon index $\Gamma \sim 1.85$ affected by a two-phase warm absorber with slightly different ionization state and column density, covering the central source in different ways; a high-column density neutral absorber intercepts a small fraction of the the central emission. The narrow Fe Kα emission line and the excess in the continuum above ~ 10 keV can be explained with a cold reflection from distant matter; the strength of this component is constant during the monitoring.

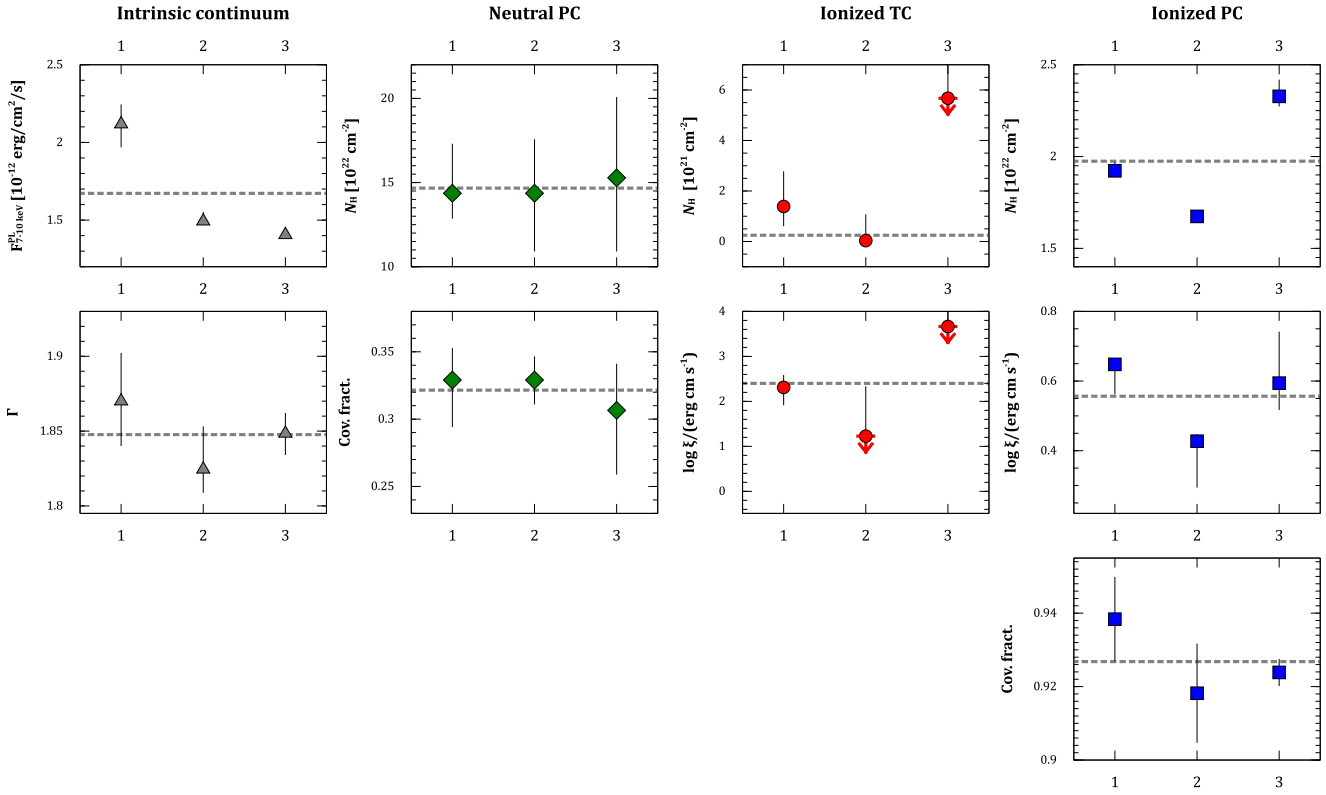

Figure 10. Evolution of spectral fit parameters versus the observation number. From left to right: intrinsic properties (grey triangles): power-law flux between 7 and 10 keV (in units of 10^{-12} ergs cm^{-2} s^{-1}) and Γ; partial covering neutral absorber (green diamonds): $N_{\rm H}$(in units of 10^{22} cm^{-2}) and covering fraction; fully covering warm absorber (red circles): $N_{\rm H}$(in units of 10^{21} cm^{-2}), log ξ; partial covering warm absorber (blue squares): $N_{\rm H}$(in units of 10^{22} cm^{-2}), log ξ, covering fraction. Dashed lines mark the mean value of each parameter.

(iv) The main driver of the observed variations is a decreasing of the direct continuum; slight variations in the partial covering ionized absorber are also detected. As regarding the total covering absorber, it is firmly detected only in the first observation; however, the data are consistent with no variation of this component. The best-fit properties derived from our analysis suggest a location of the two ionized absorbers consistent both with the BLR, the innermost part of the torus, or in between. As regards the neutral component, almost constant during the monitoring, it may either be part of the same stratified structure or associated with the walls of the torus. Based on the present data, we are not able to distinguish between the different hypotheses: a) a line of sight passing through different parts of a stratified structure of ionized gas with embedded colder and denser parts, or b) a line of sight partly intercepting the walls of the torus, providing us a favoured perspective to observe the structure of a multi-zone ionized absorber.

ACKNOWLEDGEMENTS

We are grateful to the referee for her/his constructive comments that improved the paper. We warmly thank A. Caccianiga for the useful discussions and the helpful suggestions.

Support from the Italian Space Agency is acknowledged (contract ASI INAF NuSTAR I/037/12/0).

Based on observations obtained with XMM-*Newton*, an ESA science mission with instruments and contributions directly funded by ESA Member States and the USA, NASA. This work made use of data from the *NuSTAR* mission, a project led by the California Institute of Technology, managed by the Jet Propulsion Laboratory, and funded by NASA. This research has made use of the *NuSTAR* Data Analysis Software (NuSTARDAS) jointly developed by the ASI Science Data Center and the California Institute of Technology.

This research has made use of NASA's Astrophysics Data System.

REFERENCES

Antonucci R., 1993, ARA&A, 31, 473

Arnaud K. A., 1996, in Jacoby G. H., Barnes J., eds, Astronomical Society of the Pacific Conference Series Vol. 101, Astronomical Data Analysis Software and Systems V. p. 17

Ballo L., et al., 2014, in Proceedings of Swift: 10 Years of Discovery (SWIFT 10), held 2-5 December 2014 at La Sapienza University, Rome, Italy. Online at http://pos.sissa.it/cgi-bin/reader/conf.cgi?confid=233. p. 122

Bennert N., Jungwiert B., Komossa S., Haas M., Chini R., 2006, A&A, 459, 55
Bianchi S., Maiolino R., Risaliti G., 2012, Advances in Astronomy, 2012, 782030
Blustin A. J., Page M. J., Fuerst S. V., Branduardi-Raymont G., Ashton C. E., 2005, A&A, 431, 111
Braito V., Reeves J. N., Gofford J., Nardini E., Porquet D., Risaliti G., 2014, ApJ, 795, 87
Burrows D. N., et al., 2005, Space Sci. Rev., 120, 165
Burtscher L., et al., 2013, A&A, 558, A149
Cappi M., et al., 2016, A&A, 592, A27
Cash W., Charles P., Bowyer S., 1979, A&A, 72, L6
Costantini E., 2010, Space Sci. Rev., 157, 265
Crenshaw D. M., et al., 2003, ApJ, 594, 116
Ebrero J., Costantini E., Kaastra J. S., Detmers R. G., Arav N., Kriss G. A., Korista K. T., Steenbrugge K. C., 2010, A&A, 520, A36
Ebrero J., Kaastra J. S., Kriss G. A., de Vries C. P., Costantini E., 2013, MNRAS, 435, 3028
Elitzur M., Shlosman I., 2006, ApJ, 648, L101
Goodrich R. W., 1995, ApJ, 440, 141
Harrison F. A., et al., 2013, ApJ, 770, 103
Hönig S. F., Kishimoto M., 2010, A&A, 523, A27
Jaffe W., et al., 2004, Nature, 429, 47
Kaastra J. S., et al., 2014, Science, 345, 64
Kalberla P. M. W., Burton W. B., Hartmann D., Arnal E. M., Bajaja E., Morras R., Pöppel W. G. L., 2005, A&A, 440, 775
Kallman T. R., Palmeri P., Bautista M. A., Mendoza C., Krolik J. H., 2004, ApJS, 155, 675
Kawamuro T., Ueda Y., Tazaki F., Ricci C., Terashima Y., 2016, preprint, (arXiv:1606.04941)
Keel W. C., 1996, ApJS, 106, 27
Madsen K. K., et al., 2015, ApJS, 220, 8
Malkan M. A., Gorjian V., Tam R., 1998, ApJS, 117, 25
Matt G., et al., 1996, MNRAS, 281, L69
Matt G., Fabian A. C., Guainazzi M., Iwasawa K., Bassani L., Malaguti G., 2000, MNRAS, 318, 173
McKernan B., Yaqoob T., Reynolds C. S., 2007, MNRAS, 379, 1359
Mendoza-Castrejón S., Dultzin D., Krongold Y., González J. J., Elitzur M., 2015, MNRAS, 447, 2437
Merloni A., et al., 2014, MNRAS, 437, 3550
Miniutti G., et al., 2014, MNRAS, 437, 1776
Muñoz Marín V. M., González Delgado R. M., Schmitt H. R., Cid Fernandes R., Pérez E., Storchi-Bergmann T., Heckman T., Leitherer C., 2007, AJ, 134, 648
Nandra K., O'Neill P. M., George I. M., Reeves J. N., 2007, MNRAS, 382, 194
Nenkova M., Sirocky M. M., Nikutta R., Ivezić Ž., Elitzur M., 2008, ApJ, 685, 160
Netzer H., 2013, The Physics and Evolution of Active Galactic Nuclei
Netzer H., 2015, ARA&A, 53, 365
Osterbrock D. E., 1989, Sky & Telesc., 78, 491
Palmeri P., Mendoza C., Kallman T. R., Bautista M. A., Meléndez M., 2003, A&A, 410, 359
Parker M. L., et al., 2016, MNRAS, 461, 1927
Piconcelli E., Jimenez-Bailón E., Guainazzi M., Schartel N., Rodríguez-Pascual P. M., Santos-Lleó M., 2004, MNRAS, 351, 161
Porquet D., Reeves J. N., O'Brien P., Brinkmann W., 2004, A&A, 422, 85
Proga D., Kallman T. R., 2004, ApJ, 616, 688
Reynolds C. S., Fabian A. C., Makishima K., Fukazawa Y., Tamura T., 1994, MNRAS, 268, L55
Risaliti G., 2016, Astronomische Nachrichten, 337, 529
Severgnini P., Ballo L., Braito V., Caccianiga A., Campana S., Della Ceca R., Moretti A., Vignali C., 2015, MNRAS, 453, 3611
Strüder L., et al., 2001, A&A, 365, L18
Tombesi F., Cappi M., Reeves J. N., Nemmen R. S., Braito V., Gaspari M., Reynolds C. S., 2013, MNRAS, 430, 1102
Trippe M. L., Crenshaw D. M., Deo R. P., Dietrich M., Kraemer S. B., Rafter S. E., Turner T. J., 2010, ApJ, 725, 1749
Turner M. J. L., et al., 2001, A&A, 365, L27
Wilms J., Allen A., McCray R., 2000, ApJ, 542, 914
Yaqoob T., Murphy K. D., Miller L., Turner T. J., 2010, MNRAS, 401, 411
den Herder J. W., et al., 2001, A&A, 365, L7